X-RAY MICROLENSING IN RXJ1131–1231 AND HE1104–1805

G. Chartas¹, C. S. Kochanek², X. Dai², S. Poindexter², & G. Garmire¹
Received 2008 May 24

ABSTRACT

We present results from a monitoring campaign performed with the Chandra X-ray Observatory of the gravitationally lensed quasars RX J1131–1231 and HE 1104–1805. We detect significant X-ray variability in all images of both quasars. The flux variability detected in image A of RX J1131–1231 is of particular interest because of its high amplitude (a factor of ~ 20). We interpret it as arising from microlensing since the variability is uncorrelated with that of the other images and the X-ray flux ratios show larger changes than the optical as we would expect for microlensing of the more compact X-ray emission regions. The differences between the X-ray and optical flux ratios of HE 1104–1805 are less dramatic, but there is no significant soft X-ray or dust absorption, implying the presence of X-ray microlensing in this system as well. Combining the X-ray data with the optical light curves we find that the X-ray emitting region of HE 1104–1805 is compact with a half-light radius $\lesssim 6r_g$, where the gravitational radius is $r_g=3.6\times10^{14}$ cm, thus placing significant constraints on AGN corona models. We also find that the microlensing in HE 1104–1805 favors mass models for the lens galaxy that are dominated by dark matter. Finally, we better characterize the massive foreground cluster near RX J1131–1231, set limits on other sources of extended X-ray emission, and limit the fluxes of any central odd images to be 30–50 (3 σ) times fainter than the observed images.

Subject headings: galaxies: active — quasars: individual (RX J1131–1231) — quasars: individual (HE 1104–1805) — X-rays: galaxies — gravitational lensing

1. INTRODUCTION

Resolving the emission regions of distant quasars is beyond the current capabilities of present-day telescopes, as direct imaging of accretion disks requires angular resolutions on the order of tens of nanoarcseconds at $z \sim 1$. Until the spatial resolution of telescopes reaches this limit, we will have to rely on indirect methods of mapping the emission regions of quasars. Such methods include light-travel time arguments, reverberation mapping of the broad line region (Blandford & McKee 1982; Peterson 1993, Netzer & Peterson 1997), reverberation mapping of the Fe K α emission region (Young & Reynolds 2000), occultation measurements of the central X-ray source by orbiting Compton thick clouds (Risaliti et al., 2007), and microlensing of the continuum and line emission regions (e.g., Grieger et al. 1988 and 1991; Schneider, Ehlers & Falco 1992; Gould & Gaudi 1997; Agol & Krolik 1999; Yonehara et al. 1999; Mineshige & Yonehara 1999; Chartas et al. 2002a; Popovic et al. 2003; Blackburne et al. 2006; Pooley et al. 2006, 2007; Kochanek et al. 2007; Jovanovic et al. 2008; Morgan et al. 2008a, 2008b).

We observe microlensing as uncorrelated variability in the brightnesses of the images of a lensed quasar, where the amplitude of the variability is determined by the size of the emission regions (e.g., Lewis et al. 1998; Popovic & Chartas 2005). The largest components, the radio, dust and optical line emission regions, should show little or no microlensing variability. The thermal continuum emission from the disk should show greater variability at shorter wavelengths corresponding to smaller disk radii and higher temperatures, and this has been observed by Poindexter et al. (2008) and Anguita et al. (2008). The non-thermal X-ray emission is thought to be dominated by inverse Comp-

ton scattering of UV photons from the disk (e.g., Reynolds & Nowak 2003), some of which is reprocessed into Fe K α line emission (e.g., George & Fabian 1991; Mushotzky et al. 1993) but the geometry and scale of these emission regions is not well understood.

The effects of microlensing on the X-ray fluxes of lensed images have been reported for many lenses at this point, including Q0957+561 (e.g., Chartas et al. 1995), RX J0911+0511 (e.g., Morgan et al. 2001; Chartas et al. 2001), H1413+117 (e.g., Chartas et al. 2004, 2007), PG 1115+080 (Pooley et al. 2006; Morgan et al. 2008b), and RX J1131-1231 (e.g., Blackburne et al. Kochanek et al. 2007; Dai et al. 2008). The differences between the X-ray flux ratios and optical flux ratios can be used to estimate the source size after accounting for absorption by the interstellar medium of the lens (e.g., Dai & Kochanek 2008) and the effects of substructures (satellites) in the lens halo (Mao & Schneider 1998). Pooley et al. (2007) used observed X-ray and optical flux ratios for ten four-image lensed quasars to show that the X-ray source is much more strongly microlensed than the optical source, indicating that the X-ray emission region is more compact than the optical. They also found that their estimates of the optical source sizes were significantly larger than would be expected based on the observed, magnificationcorrected optical fluxes. Morgan et al. (2008a) measured the sizes of the optical emission regions of 11 quasars using microlensing to find that the sizes scaled with black hole mass as expected from thin disk theory (Shakura & Sunyaev 1973) and had approximately the sizes expected from thin disk theory, but confirmed the Pooley et al. (2007) result that these sizes, both microlensing and theoretical. are larger than expected given the observed optical flux

Department of Astronomy & Astrophysics, Pennsylvania State University, University Park, PA 16802, chartas@astro.psu.edu

² Department of Astronomy and the Center for Cosmology and Astroparticle Physics, The Ohio State University, Columbus, OH 43210, USA

and the same disk model.

Accurate microlensing estimates of the sizes of the Xray emission regions requires X-ray light curves rather than isolated epochs. First, the absolute magnifications of lensed images are not well understood because substructure in the lens galaxy can modify the fluxes from the predictions of lens models (e.g., Mao & Schneider 1998; Dalal & Kochanek 2002). While comparing optical and X-ray flux ratios provides estimates for the difference in size between the emission regions, the lack of a secure estimate of the intrinsic flux ratios makes it difficult to set an absolute scale. Second, quasars have intrinsic variability that appears in the images with relative time delays, which means that instantaneous flux ratios are contaminated by the effects of time variability modulated by the delays. Third, while the source size ultimately determines the amplitude of microlensing variability, the instantaneous values are a combination of the source size and the location of the source in the complex microlensing magnification patterns. Monitoring the variability minimizes these problems and should lead to far more accurate estimates of the sizes.

We have been monitoring roughly 25 lenses in the optical to measure time delays (e.g., Kochanek et al. 2006) and to study quasar structure (e.g., Morgan et al. 2008a; Poindexter et al. 2008). From this sample we selected a small subset with reasonable X-ray fluxes for monitoring with the Chandra X-ray Observatory. Given a wellsampled optical light curve that can be used to determine the size of the optical/UV emission region and act as a microlensing variability "reference," we can afford to sample the X-ray microlensing variability relatively sparsely. In this paper we present the X-ray observations of the lensed quasars RX J1131–1231 ($z_s = 0.658$) and HE 1104–1805 $(z_{\rm s}=2.32)$. The optical data for RX J1131-1231 and HE 1104-1805 are presented in Morgan et al. (2006) and Poindexter et al. (2007) respectively, and the optical microlensing results are presented in Morgan et al. (2008a) and Poindexter et al. (2008). Here we carry out a microlensing analysis of HE 1104-1805, while a companion paper, Dai et al. (2009), does so for RX J1131-1231. We discuss the observations and data analysis in §2, study the microlensing of HE 1104-1805 in §3 and summarize our results in $\S 4$. Throughout this paper we adopt a Λ dominated cosmology with $H_0 = 70 \text{ km s}^{-1} \text{ Mpc}^{-1}$, Ω_{Λ} = 0.7, and $\Omega_{\rm M} = 0.3$.

2. X-RAY OBSERVATIONS AND DATA ANALYSIS

We monitored RX J1131–1231 and HE 1104–1805 with the Advanced CCD imaging Spectrometer (ACIS; Garmire et al. 2003) on board the *Chandra X-ray Observatory* (hereafter *Chandra*) using short (~ 5 ksec) snapshot observations. We obtained 5 epochs for each lens in 2006 placing the sources on the back-illuminated S3 chip of ACIS. We combined these with archival observations of RX J1131–1231 in April 2004 and HE 1104–1805 in February 2000. A log of the observations that includes observation dates, observed count rates, total exposure times, and observation identification numbers is presented in Table 1. We analyzed the data using the standard software CIAO 4.0 provided by the CXC. We used standard CXC threads to screen the data for status, grade, and time intervals of acceptable aspect solution and background lev-

els. We removed the \pm 0″.25 spatial randomization applied to the event positions by the standard pipeline and instead used the sub-pixel resolution techniques developed by Tsunemi et al. (2001) and Mori et al. (2001) in order to improve the image resolution.

The Chandra spectra of RX J1131–1231 and HE 1104–1805 were fit with a variety of models employing XSPEC version 12 (Arnaud 1996). For all spectral models of RX J1131–1231 and HE 1104–1805 we included Galactic absorption due to neutral gas (Dicky & Lockman 1990) with column densities of $N_{\rm H}=3.6\times10^{20}~{\rm cm}^{-2}$ and 4.6 \times 10²⁰ cm⁻², respectively. We use 90% confidence level uncertainties unless otherwise stated.

2.1. Spatial and Spectral Analysis

For estimating the X-ray counts of images B, C, and D of RX J1131–1231 we extracted events from circular regions with radii of 1.5 arcsec slightly off-center from the images to reduce contamination from nearby images (see panel (c) of Fig. 1). To estimate the X-ray counts of image A of RX J1131–1231, which lies between images B and C, we extracted events within a 0.75 arcsec circular region centered on A. Aperture corrections were applied to all images to account for counts not included in the extraction regions. For estimating the X-ray counts of images A and B of HE 1104-1805 we extracted events from circular regions centered on the images with radii of 1.5 arcsec. The backgrounds for RX J1131-1231 and HE 1104-1805were determined by extracting events within an annulus centered on the mean location of the images with inner and outer radii of 7.5 arcsec and 50 arcsec, respectively. Contamination between images was minimized and made insignificant by the application of the sub-pixel resolution technique and the use of appropriately sized and offcenter extraction apertures. We also corrected for "pileup," an instrumental effect that occurs when two or more X-ray photons strike individual or neighboring CCD pixels within one frame time. Neglecting these corrections can cause spectral distortion, grade migration and distortion of the image PSF. We used the forward spectral-fitting tool LYNX (Chartas et al. 2000) to estimate the fraction of events lost due to the pile-up effect.

Table 1 summarizes the observed 0.2–10 keV band source counts. The pile-up corrections needed to correctly estimate these counts can be significant. For example the counts for images B and C in the 2004 April 12 observation of RX J1131–1231 have pile-up corrections of 37% and 16% respectively. In their analysis of the 2004 observation of RX J1131–1231, Blackburne et al. (2006) did not include pile-up corrections, so our present results should be more reliable. In particular, pile-up usually leads to energy spectra that appear harder, and this likely explains the differences in the X-ray spectral hardness ratios reported by Blackburne et al. (2006) and our present results.

In Figure 1 we show the Lucy-Richardson deconvolved images in the 0.2–8 keV bandpass of the *Chandra* observations of RX J1131–1231 and HE 1104–1805. To estimate the relative X-ray image positions of RX J1131–1231 and HE 1104–1805 we modeled the *Chandra* images using point-spread functions (PSFs) generated by the simulation tool MARX (Wise et al 1997). The X-ray event locations were binned with a bin-size of 0".0246 to sample

the PSF sufficiently (an ACIS pixel subtends 0".491). The simulated PSFs were fitted to the *Chandra* data by minimizing the C-statistic formed between the observed and simulated images. In Table 2 we compare the X-ray image separations to the observed NICMOS values reported by Morgan et al. (2006) for RX J1131-1231 and by Léhar et al. (2000) for HE 1104-1805. We conclude that the X-ray and optical image positions are consistent given the estimated uncertainties.

The deconvolved images of RX J1131-1231 and HE 1104-1805 do not show any additional lensed images. To obtain quantitative limits on possible additional images located at the centers of RX J1131-1231 and HE 1104-1805 we extracted the 0.2-10 keV counts within 0.4 arcsec circles centered on the images at the mean lens position of each quasar. The backgrounds in the central source extraction regions are dominated by the contamination from the images - the instrumental and cosmic backgrounds in the 0.4 arcsec extraction circles are significantly lower than the contamination. To estimate the fractional contamination per image we used the 0.2–10 keV counts in 0.4 arcsec circular apertures placed 1 and 2 arcsec North of image B in RX J1131-1231 and 1 and 2 arcsec Northwest of image A in HE 1104-1805. The detected 0.2-10 keV counts in the central 0.4 arcsec apertures are consistent with the estimated background and contamination from the bright images.

By combining all the data for each lens we set 3σ upper limits on the 0.2–10 keV flux of any central, odd image of 1×10^{-14} and 4×10^{-15} ergs s⁻¹ cm⁻² for RX J1131–1231 and HE 1104–1805, respectively. These limits corresponded to a 3σ limit on the flux ratio of a factor of 50 relative to image C in RX J1131–1231, and a factor of 30 relative to image A in HE 1104–1805. While relatively tight, these limits are not strong enough to constrain the central surface density of the lens (Keeton 2003). For example, in the models we use for HE 1104–1805 below, the expected flux ratio between image A and any central image is $> 10^3$.

We performed fits to the individual spectra of the images of RX J1131-1231 and HE 1104-1805 using events in the 0.4–8 keV energy range with a model that consisted of a simple power law modified by Galactic absorption. Due to the moderate S/N of the spectra, we performed these fits using the Cash statistic which does not require binning of the data, although if we instead use χ^2 statistics we find similar results. The best-fit parameters of these fits and the unabsorbed 0.2-2 keV and 2-10 keV fluxes are presented in Tables 2 and 3. We found no significant variability (within the 90% errors) of the photon indices (Γ) of the spectra of the images of RX J1131-1231 and HE 1104-1805 with the exception of the 2004 observation of RX J1131–1231 that showed significant differences of Γ between images A/B/C with $\Gamma \simeq 1.44$ and image D with $\Gamma \simeq 1.95$. We also considered models that included neutral absorption at the redshifts of the sources or lenses of RX J1131-1231 and HE 1104-1805. We do not detect any additional neutral absorption at these redshifts. This is consistent with the marginal detection of absorption in HE 1104–1805 in our earlier analysis (Dai et al. 2006).

In Figure 2 we show the *Chandra* image of the 2004 observation of the lensed system RX J1131-1231 and the

surrounding field. To reduce background contamination and to enhance possible soft extended X-ray emission we filtered the image to include only photons with energies ranging between 0.4 and 3.0 keV. The image was binned with a bin size of 0.5 arcsec and adaptively smoothed with the tool CSMOOTH developed by Ebeling et al. (2000). CSMOOTH smooths a two-dimensional image with a circular Gaussian kernal of varying radius. We confirm the extended soft X-ray emission reported by Morgan et al. (2006) centered at 11 32 1.6, -12 31 6.5 (J2000) and about 158 arcsec Northeast of image D of RX J1131-1231. This emission comes from a foreground cluster at z = 0.1. Morgan et al. (2006) also reported a possible detection at a low significance level (3 σ) of extended emission centered 33 arcsec Southwest of RX J1131-1231 at 11 31 50.1, -12 32 23 (J2000). We combined all six observations of RX J1131-1231 listed in Table 1, for a total exposure time of 33.8 ksec, to better limit this possible source. All the observations from 2006 were performed in sub-array mode to mitigate pile-up and with the reduced field of view they do not include the foreground cluster to the Northeast of the lens. Figure 3 shows the adaptively smoothed image including only photons with energies from 0.4 to 3.0 keV. We find no significant sources of extended emission near the lens beyond the foreground cluster. The 0.2–2. keV 3σ upper flux and luminosity limits are 5×10^{-15} ergs cm⁻² s⁻¹ and 1.3×10^{42} ergs s⁻¹, respectively, assuming a cluster with a temperature of 1.5 keV at the lens redshift with an abundance of 0.3 solar and an extraction radius of 30 arc-

We fit the emission from the foreground cluster using a β model for the cluster brightness profile combined with a uniform background of 0.005 events per pixel. Prior to performing the fit we binned the image in 1" pixels and smoothed this with a Gaussian ($\sigma=3''$). The fits were performed with the CXC software package SHERPA. We find that the cluster center is $\Delta\alpha=150''\!.2\pm0''\!.5$ East and $\Delta\delta=52''\!.3\pm0''\!.5$ North of image D. The smoothed intensity distribution is nearly round with an ellipticity of $\epsilon=0.10\pm0.3$. The best-fit values for β and the core radius of the cluster are $\beta=0.4\pm0.2$ and $r_0=4''\!.2^{+0.4}_{-0.3}$ (8 kpc), respectively.

We extracted the spectrum of this z=0.1 cluster from a 50 arcsec radius circle centered on the X-ray cluster center. This spectrum was fit with a simple model consisting of an emission spectrum from hot diffuse gas based on the XSPEC model mekal modified by Galactic absorption. We obtain best-fit values for the temperature and metal abundances of $1.2^{+0.2}_{-0.1}$ keV and $A=0.5^{+0.5}_{-0.2}$, respectively (both errors are at the 90% confidence level). The 2–10 keV luminosity of this cluster of galaxies is 1.7×10^{42} ergs sec⁻¹. These are consistent with the Morgan et al. (2006) estimates and the values for the temperature, β and the core radius are consistent with the observed correlations of clusters (e.g. Jones & Forman 1999).

We also stacked the images of the six observations of HE 1104–1805 listed in Table 1 for a total exposure time of 71.8 ksec. Figure 4 shows the adaptively smoothed image of HE 1104–1805 including only photons with energies from 0.4 to 3.0 keV. We find no significant sources of extended emission. The 0.2–2 keV 3σ upper flux and luminosity limits are 3.4×10^{-15} ergs cm⁻² s⁻¹ and

 $5.7 \times 10^{42} \text{ ergs s}^{-1}$, respectively, assuming a cluster with a temperature of 1.5 keV at the lens redshift with an abundance of 0.3 solar and an extraction radius of 30 arcsec.

2.2. Timing Analysis

The 0.2–10 keV time-delay corrected light curves of the images of RX J1131-1231 and HE 1104-1805 are shown in Figures 5a and 5b respectively. Significant X-ray flux variability is detected in all images. RX J1131-1231 shows a mixture of intrinsic and microlensing variability. If we normalize the first epoch for image D to match the optical light curves, we find that images B, C and D roughly track the optical light curves and show similarities in their time variability. In Figure 6a we show the flux ratios F_A/F_C , F_B/F_C , and F_D/F_C in the 0.2–10 keV and R-bands of RX J1131-1231. The flux ratio F_B/F_C is almost constant in both the X-ray and optical bands indicating that the observed variability in images B and C is correlated and therefore mostly intrinsic in origin. Image A shows a completely different behavior. It is a factor of ~ 4 fainter in the X-rays than the optical relative to C/D in 2004, comparable to the optical in the spring of 2006, and a factor of ~ 5 brighter by the fall of 2006. Since the 2006 observations come in clusters with temporal separations of order the A/B/C time delays, we can be confident that these differences are not due to intrinsic variability modulated by the time delay. The significant rise of the F_A/F_C ratio in the X-ray band compared to the one measured in the Rband supports our microlensing interpretation of the flux enhancement in image A of RX J1131-1231. We note that the flux ratios reported in our analysis for the 2004 observation of RX J1131-1231 are different from those reported by Blackburne et al. (2006) because of the correction for the loss of counts due to pile-up and the correction for the spectral distortion due to pile-up. We see no strong evidence for variations in the spectral hardness, but this is a weak statement given the limited count rates.

HE 1104–1805 also affected by intrinsic X-ray variability. In particular, the peak in the optical flux near 4100 days seems likely to be associated with a peak in the X-ray flux. In Figure 6b we show the flux ratios F_A/F_B in the 0.2–10 keV and R-bands of HE 1104–1805. The February/March and October/November epochs are roughly separated by the time delay, so we can reasonably conclude that the X-ray flux ratio near 4050 days (observed A) is approximately $F_A/F_B \simeq 1$ and very different from the optical flux ratio of $F_A/F_B \simeq 3$. Since there is no evidence for significant soft X-ray or dust absorption (see §2.3, Dai et al. 2006, Poindexter et al. 2008) this difference in flux ratios must be due to microlensing. In §3 we proceed with fitting the light-curves of HE 1104-1805 with a sophisticated microlensing model. The microlensing analysis of the light-curves of RX J 1131-1231 will be presented in a companion paper by Dai et al. (2009). As with RX J1131–1231, we see no evidence for variations in the spectral hardness, largely due to the large uncertainties.

3. X-RAY MICROLENSING IN HE 1104-1805

We modeled the microlensing in HE 1104-1805 as in Morgan et al. (2008a) and Poindexter et al. (2008) using a fixed 162 day time delay, the R-band light curve

constructed from our SMARTS data (Poindexter et al. 2007), OGLE (Wyrzykowski et al. 2003), and Ofek & Maoz (2003), and the delay-corrected X-ray flux measurement. The main free parameters of our lensing model for HE 1104-1805 are the X-ray and UV (rest-frame) scale lengths, a microlens mass scale, a mass fraction of the local surface density comprised of stars, and a velocity vector describing the motion of the AGN emission region across the microlensing caustics. We used the lens model sequence from Poindexter et al. (2007), where we start from a constant mass-to-light ratio model for the mass distribution, defined by $f_{M/L} = 1$, and then reduce its mass in 10% increments while adding an NFW halo, where $f_{M/L} = 0$ would correspond to a pure halo model. The measured time delay requires $f_{M/L} \simeq 0.3$. We made 8 random realizations of the star fields near each image and then generated 8192² pixel magnification maps using the methods of Kochanek (2004). The maps had an outer scale of $10R_{\rm E}=4.3\times10^{16}$ cm and an inner scale of $10R_E/8192=4.3\times10^{13}$ cm. Based on its emission line widths, Peng et al. (2006) estimated that the black hole mass in HE 1104–1805 is $M_{\rm BH} = 2.4 \times 10^9 M_{\odot}$, corresponding to a gravitational radius of $r_{\rm g}=GM_{\rm BH}/c^2=3.6\times 10^{14}$ cm that is well-resolved in the magnification maps. We modeled the surface brightness of the emission regions as a face-on, thin disk (Shakura & Sunyaev 1973) without the central temperature depression,

whenout the central temperature depression,
$$f_{\nu} = \frac{2h_{\rm p}c}{\lambda_{rest}^3} \left[\exp\left(\frac{R}{R_{\lambda_{\rm rest}}}\right) - 1 \right]^{-1}$$
 where the scale length

$$\begin{split} R_{\lambda_{rest}} &= \left[\frac{45G\lambda_{\rm rest}^4 M_{\rm BH} \dot{M}}{16\pi^6 h_{\rm p} c^2} \right]^{1/3} \\ &= 9.7 \times 10^{15} \left(\frac{\lambda_{\rm rest}}{\mu \rm m} \right)^{4/3} \left(\frac{M_{\rm BH}}{10^9 M_{\odot}} \right)^{2/3} \left(\frac{L}{\eta L_{\rm E}} \right)^{1/3} ~{\rm cm} \end{split}$$

is the radius at which the disk temperature matches the rest wavelength of the observations, $kT = h_p c/\lambda_{rest}$, M is the accretion rate, $L/L_{\rm E}$ is the luminosity in units of the Eddington luminosity and $\eta = L/(\dot{M}c^2)$ is the accretion efficiency. We scale the results assuming a radiative efficiency of $\eta = 10\%$. While the available energy of accretion is larger, the division of that energy between radiative, advective and kinetic losses is not directly calculable at present. Studies of the growth of black holes tend to find that the average radiative efficiency of accretion is less than 10% (e.g. Shankar et al. 2007), and low radiative efficiencies are also needed to reconcile thin disk theory with microlensing accretion disk size estimates (e.g., Morgan et al. 2007).

For the UV (rest-frame) emission we can neglect the central temperature depression provided $R_{\lambda_{\text{rest}}} >> R_{in}$ where $R_{in} \simeq 2r_g$ is the inner edge of the disk. While this thermal accretion disk model is not appropriate for the non-thermal X-ray emission, Mortonson et al. (2005) have shown that microlensing essentially measures the half-light radius of the emission region, so we used the same profile for the X-rays to simplify the computations but regard it as a measurement of the half-light radius $R_{1/2} = 2.44R_{\lambda}$. The microlenses were given a power-law mass distribution $dN/dM \propto M^{-1.3}$ with a dynamic range in mass of a factor of 50, roughly matching the Galactic disk mass function of Gould (2000), and we use a uniform prior on the mean microlens mass of $0.1 M_{\odot} \leq \langle M \rangle \leq M_{\odot}$. We modeled the probability distribution for the physical velocities as in Poindexter et al. (2008) where our projected velocity onto the lens plane is 73 km/s, the velocity dispersion of the lens is 308 km/s based on the critical radius of the mass model, and the lens and source have rms peculiar velocities of 153 and 71 km/s respectively. The data were then modeled using the Bayesian Monte Carlo method of Kochanek (2004).

The microlensing data constrains the source velocity and size in "Einstein" length units of $\langle M \rangle^{1/2}$ cm. We can determine the true sizes using the prior on the microlens masses, the prior on the physical velocities or both. Figure 7 shows the probability distribution found for $\langle M \rangle$ assuming the prior on the physical velocities. While the distribution peaks at somewhat lower mass ($\sim 0.05 M_{\odot}$) than the range of our prior $(0.1M_{\odot} \text{ to } 1.0M_{\odot})$, the distribution is so broad $(0.005M_{\odot} \text{ to } 0.9M_{\odot} \text{ at } 1\text{-}\sigma)$ that we can view them as statistically consistent. For example, none of the results depend significantly on the inclusion of the mass prior. Since the mass scales as $\langle M \rangle \propto v_e^2/\hat{v}_e^2$ where v_e is the physical velocity from the prior and \hat{v}_e is the Einstein-unit velocity estimated from the microlensing models, it is difficult to tightly constrain the mean mass with a single lens given the unknown peculiar velocities of the lens and source even with perfect knowledge of the Einstein-unit velocity.

Figure 8 shows the raw estimates of the source sizes \hat{r}_s in Einstein units, where $r_s = \hat{r}_s \langle M/M_{\odot} \rangle^{1/2}$. Both of these are scaled source sizes R_{λ} defined by the emission profile presented earlier in this section. The consequence of adding the prior on the microlens masses is to drive the source sizes \hat{r}_s to be modestly smaller. In essence, a given level of microlensing variability can be created by a large source moving rapidly (big \hat{r}_s and \hat{v}_e) or a small source moving more slowly (small \hat{r}_s and \hat{v}_e). But high effective velocities correspond to small mass scales given a fixed physical velocity, so imposing the mass prior given the distribution seen in Figure 7 will favor lower velocities \hat{v}_e and smaller sources \hat{r}_s . It will have less effect on the physical source size $r_s = \hat{r}_s \langle M/M_{\odot} \rangle^{1/2}$ because the smaller size \hat{r}_s is balanced by the larger mass scale $\langle M/M_{\odot} \rangle$ (see Kochanek 2004). While Figure 8 truncates the probability distribution for the X-ray source at the pixel scale of the magnification patterns, it would not converge to zero if we used magnification patterns with smaller pixel scales to extend the distribution to smaller source sizes. This is a consequence of not having a well-sampled X-ray light curve. The source must be small enough to allow the Xray flux ratio to differ from the optical, but still smaller sources are disfavored because even more discrepant flux ratios become more likely. However, reducing the size still further has no effect on the probabilities because it converges to the likelihood of the data points avoiding precise caustic crossings. Unfortunately, this does mean that we will obtain robust upper limits on the X-ray source size but not lower limits.

Figure 9 shows the results for the rest-frame UV and X-ray source sizes R_{λ} assuming either uniform or logarithmic priors for the size. We used R_{λ} for both so that the sizes are easily compared. If we regard the source

size at 2000Å as measuring a projected area, then R_{λ} scales as $(\cos i)^{-1/2}$ for inclination angle i of a thin inclined accretion disk. Similarly, the X-ray size in Figure 9 should be increased by a factor of 2.44 to convert from R_{λ} to the half-light radius $R_{1/2}$. The disk size at 2000Å (R-band in the rest frame at $z_s = 2.32$) is $15.6 \leq \log(R_{200}\sqrt{\cos(i)}/\text{cm}) \leq 16.2$ for a logarithmic prior on the size and $15.8 \leq \log(R_{200}\sqrt{\cos(i)}/\text{cm}) \leq 16.3$ for a linear prior on the size. This agrees well with our earlier estimates in Poindexter et al. (2008) and Morgan et al. (2008a). The X-ray size is less certain and more prior-dependent, with an estimated half-light radius $14.2 \leq \log(R_{X,1/2}/\text{cm}) \leq 15.0$ for a logarithmic prior on the size and 14.6 $\leq \log(R_{X,1/2}/\text{cm}) \leq 15.3$ for the linear prior on the size. We note that the difference in the sizes is entirely driven by the significant differences between the X-ray and optical flux ratios at the time of the X-ray observation.

The microlensing data also prefer lens models with low stellar mass fractions, as shown in Figure 10.The probability distribution peaks at $f_{M/L} \simeq 0.2$, in relatively good agreement with the value of $f_{M/L} = 0.3$ that agrees best with the measured time delay and a Hubble constant of $H_0 = 72 \text{ km s}^{-1} \text{ Mpc}^{-1}$. While this preliminary result does not lead to a microlensing constraint on $f_{M/L}$ that is tight enough to break the degeneracies between the radial mass distribution and the Hubble constant (see Kochanek 2002), it is encouraging that there is agreement with the time delays given the expected value of H_0 and that the microlensing requires a dark matter-dominated mass distribution. A detailed microlensing analysis of RX J1131–1231 that provides similar constraints on the structure of the lens and the structure of the quasar is presented in Dai et al. (2009).

Figures 11 and 12 show an example of a trial that fits the data well. In this trial the Einstein unit source sizes are $\log R_{\lambda} = 14.2$ and 16.2 for the X-ray and UV rest-frame sources respectively and the effective velocity corresponds to a sensible microlens mass scale. We chose this solution mainly because of the curious origin of the initial R-band peak, where what might be interpreted as a single heavily smoothed caustic crossing is actually a pair of competing caustic crossings in the A and B images, where the A image dominates because of its shallower magnification gradients. The X-ray epoch then corresponds to time when the source is in a valley between caustics in both images. We note that this particular solution probably would not reproduce the wavelength dependence of the optical and IR flux ratios in HE 1104-1805 discussed and modeled Poindexter et al. (2008).

4. DISCUSSION AND CONCLUSIONS

While there is a consensus that the origin of the keV X-ray continuum emission from quasars is inverse Compton scattering (e.g., see the review of Reynolds & Nowak 2003), the extent and geometric configuration of the emission region is less clear. In the standard disk-corona model (e.g., Haardt & Maraschi 1991; Merloni 2003), it is produced in a hot, extended corona surrounding the disk. In the general relativistic MHD simulations of Hirose et al. (2004, also Machida & Matsumoto 2003) the region of the corona with the highest current densities lies close to the

inner edge of the disk. Under the assumption that these are also the regions with the highest dissipation rates for heating the corona (see Hirose et al. 2004), they will dominate the X-ray emission and we would expect the X-ray source size to track the inner edge of the disk.

Microlensing of the X-ray source allows us to observationally measure the size of the X-ray emission region. We start with well-sampled optical light curves that allow us to determine the size of the accretion disk. Morgan et al. (2008a) found a clear scaling of the disk size with black hole mass that is consistent with the $M_{BH}^{2/3}$ scaling of simple thin disk theory for a fixed Eddington accretion rate (Shalung & Shalung & (Shakura & Sunvaev 1973). We can estimate the disk size by two routes other than microlensing. First we can estimate it from the observed flux at some wavelength. Size estimates from the observed flux do not depend on the black hole mass but depend only on the assumed temperature profile and the assumption that the disk radiates as a black body at that temperature. Second, thin disk theory predicts the scale length through the expression we presented in the beginning of §3. Size estimates from thin disk theory depend on the black-hole mass, the Eddington factor and the wavelength. The disk size from our microlensing analysis is roughly consistent with thin disk theory if the accretion efficiency is relatively low, but both the microlensing and theoretical sizes are significantly larger than that estimated from the observed optical flux of the quasar and the same disk model. This mismatch between the sizes estimated from microlensing and from the flux was first pointed out by Pooley et al. (2007). One solution to this problem may be to use a shallower temperature profile than the $T \propto R^{-3/4}$ of simple thin disk theory, and Poindexter et al. (2008) found some evidence for a shallower profile in HE 1104-1805 by examining the optical/near-IR wavelength dependence of microlensing in this system.

Our X-ray monitoring observations of RX J1131-1231 and HE 1104–1805 show significant flux variability in all images of both quasars. The factor of ~ 20 X-ray flux variability in image A of RX J1131-1231 is interesting not only because of the high amplitude but also because it is a highly magnified saddle point image. Schechter & Wambsganss (2002) pointed out that in a dark matter dominated galaxy, microlensing is in a regime where images at minima and saddle points of the time-delay surface behave differently. In particular, the saddle point images should show significantly higher variability amplitudes, just as we observe in RX J1131–1231. The relatively large sizes of accretion disks in the optical relative to the typical Einstein radius of the stars seems to have masked much of this effect in the optical signatures of microlensing – for example, where the X-ray flux ratio F_A/F_C changed by a factor of 4 during our monitoring period, the optical flux ratio changed by only a factor of 1.4. The differences between the X-ray and optical flux ratios of HE 1104-1805 also imply the presence of X-ray microlensing. Neither system shows evidence for soft X-ray or dust absorption that could explain the differences.

While we measure the source sizes by modeling the data in detail, the essence of the measurement is comparing the amplitude of the X-ray microlensing variability to that in the optical. If the amplitude for the X-ray microlensing

is larger than in the optical, then the X-ray source must be more compact, and this is what we observed in both RX J1131-1231 and HE 1104-1805. Given the estimated black hole mass of $M_{BH} = 2.4 \times 10^9 M_{\odot}$ (Peng et al. 2006), our fits to the X-ray and optical light curves using the microlensing model described in §2.5 indicate that the X-ray emission in HE 1104–1805 comes from a region smaller than $\sim 6r_g$ and the UV emission region has a size of $\sim 30r_q$. We note that the source sizes of HE 1104–1805 were derived using a Bayesian analysis which requires a prior. As shown in Figures 8 and 9 our upper limit on the X-ray source size is robust to prior selection but not the lower limit. Obtaining a more precise X-ray size estimate requires a more extensive X-ray light curve for the system. This is somewhat challenging for HE 1104–1805 because the long time delay of HE 1104-1805 (162 days, Morgan et al. 2008a) and the intrinsic variability we observe here means that this lens requires observations separated by the time delay in order to correct for intrinsic variability. This is less of a problem for almost all other candidates for Xray monitoring because they have far shorter time delays. For example, in RX J1131-1231 we observe some intrinsic variability but it is significant only on time scales much longer than the delays between the A/B/C images. Given the Morgan et al. (2008b) estimates for PG 1115+080, the Dai et al. (2009) results for RX J1131-1231, and our present results for HE 1104-1805, the X-ray microlensing results suggest that the size of the X-ray emission arises from close to the inner edge of the disk. Thus, our estimated sizes for the X-ray and UV emission regions place significant constraints on AGN models that assume extended coronal envelopes around accretion disks. Reducing the uncertainties in these measurements and measuring the scaling of the size with the estimated masses of the black holes requires longer X-ray time series and more systems, but there is clearly no technical barrier to making the measurements and extending them to the dependence of the size on X-ray energy.

Combining the data from the time series also allows us to search for extended emission from groups or clusters near the lens, which can be important for lens models (e.g. Williams et al. 2006, Fassnacht et al. 2007). Here we analyzed the X-ray data for the foreground cluster found near RX J1131–1231 by Morgan et al. (2006) in more detail, and set limits on the presence of any other clusters near both systems (see §2.4). We also used the combined images to search for central or odd images, although this is challenging given the resolution of *Chandra* and the expected faintness of the images. While we reached 1σ limits on the flux ratios of > 100, significant constraints on the central images require limits better by another order of magnitude (Keeton 2003).

We acknowledge financial support from NASA via the Smithsonian Institution grant SAO SV4-74018. CSK acknowledges financial support from NSF grant AST-0708082 and Chandra grants G06-7093 and GO7-8104.

REFERENCES

- Agol, E., & Krolik, J. 1999, ApJ, 524, 49
- Anguita, T., Schmidt, R.W., Turner, E.L., Wambsganss, J., Webster, R.L., Loomis, K.A., Long, D., & McMillan, R., 2008, A&A, 480, 327
- Arnaud, K. A. 1996, ASP Conf. Ser. 101: Astronomical Data Analysis Software and Systems V, 5, 17
- Blackburne, J. A., Pooley, D., & Rappaport, S. 2006, ApJ, 640, 569
- Blandford, R. D., & McKee, C. F. 1982, ApJ, 255, 419
- Chartas, G., et al. 2000, ApJ, 542, 655
- Chartas, G., Agol, E., Eracleous, M., Garmire, G., Bautz, M. W., & Morgan, N. D. 2002a, ApJ, 68, 509
- Chartas, G., Gupta, V., Garmire, G., Jones, C., Falco, E. E., Shapiro, I. I., & Tavecchio, F. 2002b, ApJ, 565, 96
- Chartas, G., Dai, X., Gallagher, S. C., Garmire, G. P., Bautz, M. W., Schechter, P. L., & Morgan, N. D. 2001, ApJ, 558, 119
- Chartas, G., Eracleous, M., Agol, E., & Gallagher, S. C. 2004, ApJ, 606, 78
- Chartas, G., Eracleous, M., Dai, X., Agol, E., & Gallagher, S. 2007, ApJ, 661, 678
- Chartas, G., Falco, E., Forman, W., Jones, C., Schild, R., & Shapiro, I. 1995, ApJ, 445, 140
- Dai, X., Kochanek, C.S., Chartas, G., & Mathur, S., 2006, ApJ, 637, 53
- Dai, X., & Kochanek, C.S., 2008, ApJ submitted [arXiv:0803.1679]
- Dalal, N., & Kochanek, C. S. 2002, ApJ, 572, 25
- Dickey, J. M., & Lockman, F. J. 1990, ARA&A, 28, 215
- Fassnacht, C.D., Kocevski, D.D., Auger, M.W., Lubin, L.M., Neureuther, J.L., Jeltema, T.E., Mulchaey, J.S., & McKean, J.P., 2007, ApJ submitted [arXiv:0711.2066]
- Garmire, G. P., Bautz, M. W., Ford, P. G., Nousek, J. A., & Ricker, G. R. 2003, Proc. SPIE, 4851, 28

- George, I. M., & Fabian, A. C. 1991, MNRAS, 249, 352
- Gould, A., & Gaudi, B. S. 1997, ApJ, 486, 687
- Gould, A., 2000, ApJ, 535, 928
- Grieger, B., Kayser, R., & Refsdal, S. 1988, A&A, 194, 54
- Grieger, B., Kayser, R., & Schramm, T. 1991, A&A, 252, 508
- Haardt, F., & Maraschi, L., 1991, ApJ, 380, 51
- Hirose, S., Krolik, J., De Villiers, J.-P., & Hawley, J., 2004, ApJ, 606, 1083
- Jones, C., & Forman, W. 1999, ApJ, 511, 65
- Jovanović, P., Zakharov, A. F., Popović, L. Č., & Petrović, T. 2008, MNRAS, 386, 397
- Keeton, C.R., 2003 ApJ, 582 17
- Kochanek, C. S., Dai, X., Morgan, C., Morgan, N., Poindexter, S. C. G. & Chartas, G., 2007, Statistical Challenges in Modern Astronomy IV, 371, 43
- Kochanek, C.S., Morgan, N.D., Falco, E.E., et al., 2006, ApJ, 640, 47
- Kochanek, C. S. 2002, ApJ, 578, 25
- Kochanek, C. S. 2004, ApJ, 605, 58
- Lehár, J., et al. 2000, ApJ, 536, 584
- Lewis, G. F., Irwin, M. J., Hewett, P. C., & Foltz, C. B. 1998, MNRAS, 295, 573
- Machida, M., & Matsumoto, R., 2003, ApJ, 585, 429
- Mao, S., & Schneider, P. 1998, MNRAS, 295, 587
- Merloni, A., 2003, MNRAS, 341, 1051
- Mineshige, S., & Yonehara, A. 1999, PASJ, 51, 497
- Morgan, N. D., Chartas, G., Malm, M., Bautz, M. W., Burud, I., Hjorth, J., Jones, S. E., & Schechter, P. L. 2001, ApJ, 555, 1
- Morgan, N. D., Kochanek, C. S., Falco, E. E., & Dai, X. 2006, ArXiv Astrophysics e-prints, arXiv:astro-ph/0605321
- Morgan, C. W., Eyler, M. E., Kochanek, C. S., Morgan, N. D., Falco, E. E., Vuissoz, C., Courbin, F., & Meylan, G., 2008, ApJ, 676,

80

- Morgan, C. W., Eyler, M. E., Kochanek, C. S., Morgan, N. D., Falco, E. E., Vuissoz, C., Courbin, F., & Meylan, G. 2008a, ApJ, 676, 80
- Morgan, C. W., Kochanek, C. S., Morgan, N. D., & Falco, E. E. 2007, ArXiv e-prints, 707, arXiv:0707.0305
- Morgan, C. W., Kochanek, C. S., Dai, X., Morgan, N. D., & Falco, E. E. 2008b, ArXiv e-prints, 802, arXiv:0802.1210
- Mori, K., Tsunemi, H., Miyata, E., Baluta, C., Burrows, D. N., Garmire, G. P., & Chartas, G. 2001, in ASP Conf. Ser. 251, New Century of X-Ray Astronomy, ed. H. Inoue & H. Kunieda (San Francisco: ASP), 576
- Mortonson, M.J., Schechter, P.L., & Wambsganss, J., 2005, ApJ, 628, 594
- Mushotzky, R. F., Done, C., & Pounds, K. A. 1993, ARA&A, 31, 717
- Netzer, H., & Peterson, B. M. 1997, Astronomical Time Series, 218, 85
- Ofek, E.O. & Maoz, D., 2003, ApJ, 594, 101
- Peng, C.Y., Impey, C.D., Rix, H.-W., Kochanek, C.S., Keeton, C.R., Falco, E.E., Léhar, J., & Mcleod, B.A., 2006, ApJ 649, 616
- Peterson, B. M. 1993, PASP, 105, 247
- Poindexter, S., Morgan, N., Kochanek, C.S., & Falco, E.E., 2007, ApJ, 660, 146
- Pointdexter, S. Mogan, N., & Kochanek, C.S., 2008, ApJ, 673, 34
- Pooley, D., Blackburne, J. A., Rappaport, S., Schechter, P. L., & Fong, W.-f. 2006, ApJ, 648, 67
- Pooley, D., Blackburne, J. A., Rappaport, S., & Schechter, P. L. 2007, ApJ, 661, 19
- Popović, L. Č., & Chartas, G. 2005, MNRAS, 357, 135
- Popović, L. Č., Mediavilla, E. G., Jovanović, P., & Muñoz, J. A. 2003, A&A, 398, 975
- Reynolds, C.S. & Nowak, M.A., 2003, PhR, 377, 389
- Risaliti, G., Elvis, M., Fabbiano, G., Baldi, A., Zezas, A., & Salvati, M. 2007, ApJL, 659,

L111

- Schechter, P. L., & Wambsganss, J. 2002, ApJ, 580, 685
- Schneider, P., Ehlers, J., & Falco, E. E. 1992, Gravitational Lenses, XIV, Springer-Verlag Berlin Heidelberg New York. Also Astronomy and Astrophysics Library.
- Shankar, F., Weinberg, D. H., & Miralda-Escude', J. 2007, ArXiv e-prints, 710, arXiv:0710.4488
- Tsunemi, H., Mori, K., Miyata, E., Baluta, C., Burrows, D. N., Garmire, G. P., & Chartas, G. 2001, ApJ, 554, 496
- Williams, K.A., Momchemva, I., Keeton, C.R., Zabludoff, AI., & Léhar, J., 2006, ApJ, 646,
- Wise, M. W., Davis, J. E., Huenemoerder, Houck, J. C., Dewey, D. Flanagan, K. A., and Baluta, C. 1997, *The MARX 3.0 User Guide, CXC Internal Document* available at http://space.mit.edu/ASC/MARX/
- Wryzkwoski, L., et al., 2003 Acta Astron. 53 229
- Yonehara, A., Mineshige, S., Fukue, J., Umemura, M., & Turner, E. L. 1999, A&A, 343, 41
- Young, A. J., & Reynolds, C. S. 2000, ApJ, 529, 101

 $\begin{array}{c} \text{TABLE 1} \\ \text{Log of Observations of Quasars RX J1131}{-1231} \text{ and HE } 1104{-1805} \end{array}$

Epoch	Observation Date	Chandra Observation ID	Exposure Time (ks)	$N_{ m A}{}^{ m a}$ counts	$N_{ m B}{}^{ m a}$ counts	$N_{ m C}^{ m a}$ counts	$N_{ m D}^{ m a}$ counts
Observations of RX J1131-1231							
1	2004 April 12	4814	10.	425 ± 22	2950 ± 54	839 ± 29	211 ± 15
2	2006 March 10	6913	4.9	393 ± 20	624 ± 25	204 ± 14	103 ± 10
3	2006 March 15	6912	4.4	381 ± 20	616 ± 25	233 ± 15	93 ± 10
4	2006 April 12	6914	4.9	413 ± 20	507 ± 23	146 ± 12	131 ± 12
5	2006 November 10	6915	4.8	3708 ± 61	1411 ± 38	367 ± 19	155 ± 13
6	2006 November 13	6916	4.8	3833 ± 62	1618 ± 40	415 ± 20	115 ± 11
Observations of HE 1104-1805							
1	2000 June 10	375	47.4	1024 ± 32	547 ± 23		
2	2006 February 16	6918	5.0	38 ± 6	86 ± 9		
3	2006 March 15	6917	4.6	40 ± 6	59 ± 8		
4	2006 April 09	6919	4.9	33 ± 6	61 ± 8		
5	2006 October 31	6920	5.0	60 ± 8	40 ± 6		
6	2006 November 08	6921	4.9	52 ± 7	57 ± 8		

^aBackground-subtracted source counts for events with energies in the 0.2–10 keV band. The counts for images B and C for the 2004 April 12 observation of RX J1131–1231 are corrected for pile-up by factors of 37% and 16%, respectively. The counts for images A and B for the 2006 November 10 observation of RX J1131–1231 are corrected for pile-up by factor of 32% and 13%, respectively. The counts for images A and B for the 2006 November 13 observation of RX J1131–1231 are corrected for pile-up by factors of 33% and 17%, respectively.

TABLE 2 OPTICAL AND X-RAY OFFSETS OF RX J1131–1231 AND HE 1104–1805 IMAGES

Telescope	$\Delta \alpha("), \Delta \delta(")$	$\Delta \alpha(''), \Delta \delta('')$	B $\Delta \alpha(''), \Delta \delta('')$	D	
	$\Delta \alpha(), \Delta \delta()$	$\Delta \alpha(), \Delta \delta()$	$\Delta \alpha(), \Delta \delta()$	$\Delta \alpha(), \Delta \delta()$	
RX J1131-1231 Image Offsets					
$_{ m HST}$	0,0	$0.588\pm0.003, 1.120\pm0.003$	$0.618 \pm 0.003, 2.307 \pm 0.003$	$-2.517\pm0.003, 1.998\pm0.003$	
Chandra	0,0	$0.59\pm0.02,\ 1.12\pm0.02$	$0.62\pm0.02,\ 2.31\pm0.02$	$-2.52\pm0.02,\ 2.00\pm0.02$	
HE 1104-1805 Image Offsets					
HST	_	0,0	$2.901\pm0.003, -1.332\pm0.003$	_	
Chandra	_	0,0	$2.92\pm0.02, -1.33\pm0.02$	_	

TABLE 3 RESULTS FROM FITS TO THE $\it Chandra$ IMAGE SPECTRA OF RX J1131–1231

Encol	Dama mantan ^d	Values For	Values Fan	Values For	Values For
Epoch	Parameter ^a	Values For Image A ^b	Values For Image B ^b	Image C^b	Image D^b
		Ü			_
1	Γ	$1.44_{-0.08}^{+0.08}$ $1.4_{-0.2}^{+0.2}$ $2.7_{-0.4}^{+0.4}$	$1.41^{+0.07}_{-0.07}$	$1.47_{-0.12}^{+0.12} \\ 3.1_{-0.5}^{+0.5} \\ 3.8_{-0.5}^{+0.6} \\ 5.92/797$	$1.95_{-0.20}^{+0.21}$ $0.9_{-0.2}^{+0.2}$ $0.7_{-0.2}^{+0.2}$ $2.02/707$
	$0.2-2 \text{ keV Flux } (10^{-13} \text{ erg s}^{-1} \text{ cm}^{-2})$	$1.4^{+0.2}$	$9.1^{+0.8}_{-0.8}$	$3.1^{+0.5}$	$0.9^{+0.2}$
	$2-10 \text{ keV Flux } (10^{-13} \text{ erg s}^{-1} \text{ cm}^{-2})$	$2.7^{+0.4}$	$15.7^{+1.4}_{-1.4}$	$3.8^{+0.6}$	$0.7^{+0.2}$
	C-statistic/nbins	556/787	661/787	583/787	368/787
	χ^2/ u	25/31	105/97	28/41	15.4/15
	$P(\chi^2/ u)^c$	0.76	0.27	0.95	0.42
2	Г	$1.58_{-0.15}^{+0.15} \\ 2.9_{-0.6}^{+0.6} \\ 4.5_{-0.9}^{+1.2}$	$1.63_{-0.11}^{+0.11} \\ 5.0_{-0.8}^{+0.8} \\ 7.0_{-1.1}^{+1.2}$	$1.62_{-0.19}^{+0.19} \\ 1.3_{-0.3}^{+0.3} \\ 2.3_{-0.6}^{+0.7}$	$1.66^{+0.28}_{-0.27} \\ 0.8^{+0.4}_{-0.4} \\ 1.1^{+0.5}_{-0.4}$
	$0.2-2 \text{ keV Flux } (10^{-13} \text{ erg s}^{-1} \text{ cm}^{-2})$	$2.9^{+0.6}$	$5.0^{+0.8}$	$1.3^{+0.3}$	$0.8^{+0.4}$
	$2-10 \text{ keV Flux } (10^{-13} \text{ erg s}^{-1} \text{ cm}^{-2})$	4 5 + 1.2	$7.0^{+1.2}$	$2.3^{+0.7}$	1 1 + 0.5
	C-statistic/nbins	531/838	653/838	$\frac{2.5}{-0.6}$ $\frac{435}{838}$	$\frac{1.1}{-0.4}$ $300/838$
		33/28	61/52	14.4/16	2.4/6
	$rac{\chi^2/ u}{P(\chi^2/ u)^c}$	0.24	0.18	0.57	0.9
3	Γ	$1.61^{+0.15}_{-0.15}$	$1.73^{+0.11}_{-0.11}$	$1.57^{+0.18}_{-0.18}$	$1.60^{+0.28}_{-0.28}$
	$0.2-2 \text{ keV Flux } (10^{-13} \text{ erg s}^{-1} \text{ cm}^{-2})$	$3.1_{-0.6}^{+0.13}$ $4.6_{-0.9}^{+1.2}$	$5.6^{+1.5}$	$1.8_{-0.5}^{+0.18}$ $3.0_{-0.8}^{+0.9}$	$0.8^{+0.4}_{-0.3}$ $1.2^{+0.6}_{-0.5}$
	$2-10 \text{ keV Flux } (10^{-13} \text{ erg s}^{-1} \text{ cm}^{-2})$	$4.6^{+1.2}$	$5.6_{-1.5}^{+1.5} \\ 6.7_{-1.2}^{+1.3}$	$3.0^{+0.9}$	$1.2^{+0.6}$
	C-statistic/nbins	521/838	555/838	425/838	292/838
	χ^2/ν	26/27	42/48	18.5/17	3.8/6
	$rac{\chi^2/ u}{P(\chi^2/ u)^c}$	0.52	0.73	0.36	0.7
4	Γ	$1.53^{+0.14}_{-0.14}$	$1.64^{+0.12}_{-0.12}$	$1.70^{+0.23}_{-0.23}$	$1.62^{+0.24}_{-0.24}$
	$0.2-2 \text{ keV Flux } (10^{-13} \text{ erg s}^{-1} \text{ cm}^{-2})$	$3.0^{+0.6}$	$3.9^{+0.7}$	$1.2^{+0.4}$	$1.0^{+0.4}$
	$2-10 \text{ keV Flux } (10^{-13} \text{ erg s}^{-1} \text{ cm}^{-2})$	$3.0^{+0.6}_{-0.6}$ $5.1^{+1.1}_{-1.0}$	$3.9^{+0.7}_{-0.7}$ $5.4^{+1.2}_{-1.0}$	$1.5^{+0.6}_{-0.5}$	$1.5^{+0.6}_{-0.5}$
	C-statistic/nbins	541/838	548/838	333/838	350/838
	χ^2/ u	27/29	40/41	7.7/10	13/9
	$P(\chi^2/\nu)^c$	0.58	0.52	0.66	0.15
5	Γ	$1.59^{+0.07}_{-0.07}$	$1.82^{+0.08}_{-0.09}$	$1.90_{-0.15}^{+0.15} \\ 3.4_{-0.5}^{+0.5} \\ 2.8_{-0.6}^{+0.7}$	$1.54_{-0.22}^{+0.22} \\ 1.1_{-0.3}^{+0.3}$
	$0.2-2 \text{ keV Flux } (10^{-13} \text{ erg s}^{-1} \text{ cm}^{-2})$	29^{+2}_{-2}	13^{+1}_{-1}	$3.4^{+0.5}_{-0.5}$	$1.1^{+0.3}_{-0.3}$
	$2-10 \text{ keV Flux } (10^{-13} \text{ erg s}^{-1} \text{ cm}^{-2})$	35^{+3}_{-4}	$11^{+\frac{1}{2}}_{-1}$	$2.8^{+0.7}$	$1.1_{-0.3} \\ 1.9_{-0.5}^{+0.6}$
	C-statistic/nbins	771/838	626/838	502/838	402/838
	$rac{\chi^2/ u}{P(\chi^2/ u)^c}$	72/59	66/63	34/28	7/11
	$P(\chi^2/\nu)^c$	0.1	0.37	0.19	0.7
6	Γ	$1.51^{+0.07}_{-0.07}$	$1.82^{+0.08}_{-0.08}$	$1.76^{+0.14}_{-0.14}$	$2.28^{+0.29}_{-0.28}$
	$0.2-2 \text{ keV Flux } (10^{-13} \text{ erg s}^{-1} \text{ cm}^{-2})$	30^{+2}_{-2}	15^{+2}_{-2}	$3.2^{+0.5}_{-0.5}$ $3.6^{+0.9}_{-0.8}$	$1.4_{-0.5}^{+0.5} \\ 0.6_{-0.2}^{+0.3}$
	$2-10 \text{ keV Flux } (10^{-13} \text{ erg s}^{-1} \text{ cm}^{-2})$	36^{+3}_{-3}	13^{+2}_{-2}	$3.6_{-0.8}^{+0.9}$	$0.6^{+0.3}_{-0.2}$
	C-statistic/nbins	768/838	658/838	489/838	276/838
	$rac{\chi^2/ u}{P(\chi^2/ u)^c}$	65/59	62/70	29/33	9/8
	$P(\chi^2/ u)^c$	0.29	0.76	0.66	0.36

 $[^]a$ Model 1 consists of a power-law modified by Galactic absorption. b All errors are for 90% confidence unless mentioned otherwise with all parameters taken to be of interest except absolute normalization. $^cP(\chi^2/\nu)$ is the probability of exceeding χ^2 for ν degrees of freedom if the model is correct.

TABLE 4 RESULTS FROM FITS TO THE $\it Chandra$ IMAGE SPECTRA OF HE 1104–1805

Epoch	Parameter ^a	Values For	Values For
		Image A^b	Image B^b
1	Г	$1.59^{+0.08}_{-0.08}$	$1.86^{+0.12}_{-0.12}$
-	$0.2-2 \text{ keV Flux } (10^{-14} \text{ erg s}^{-1} \text{ cm}^{-2})$	6.0 ^{+0.6}	$^{1.00}_{-0.12}_{4.20}$
		$6.9^{+0.6}_{-0.6}$	$4.28^{+0.6}_{-0.6}$
	$2-10 \text{ keV Flux } (10^{-14} \text{ erg s}^{-1} \text{ cm}^{-2})$	$10.6^{+0.2}_{-0.1}$	$3.97^{+0.7}_{-0.8}$
	C-statistic/nbins	623/790	
2	Γ	$1.4^{+0.4}_{-0.4}$	$1.6^{+0.3}_{-0.3}$
	$0.2-2 \text{ keV Flux } (10^{-14} \text{ erg s}^{-1} \text{ cm}^{-2})$	$2.6_{-1.6}^{+1.8}$	$6.5^{+3.0}_{-2.7}$
	$2-10 \text{ keV Flux } (10^{-14} \text{ erg s}^{-1} \text{ cm}^{-2})$	$5.8_{-3.5}^{-1.6}$	$10.2^{-2.7}_{-4.0}$
	C-statistic/nbins	192/838	284/1060
	,	,	,
3	Γ	$1.53^{+0.40}_{-0.41}$	$2.4^{+0.4}_{-0.4}$
	$0.2-2 \text{ keV Flux } (10^{-14} \text{ erg s}^{-1} \text{ cm}^{-2})$	$3.4^{+2.2}_{-2.3}$	$8.4^{+3.8}_{-4.1}$
	$2-10 \text{ keV Flux } (10^{-14} \text{ erg s}^{-1} \text{ cm}^{-2})$	$5.9_{-3.0}^{+4.0}$	$3.0_{-1.5}^{+2.3}$
	C-statistic/nbins	186/838	195/1060
4	Г	$1.76^{+0.50}_{-0.47}$	$2.03^{+0.37}_{-0.36}$
-1	$0.2-2 \text{ keV Flux } (10^{-14} \text{ erg s}^{-1} \text{ cm}^{-2})$	$0.70_{-0.47}$	2.03 _{-0.36} 6 = +3.3
		$2.9^{+2.3}_{-1.9}$	$6.5^{+3.3}_{-2.7}$
	$2-10 \text{ keV Flux } (10^{-14} \text{ erg s}^{-1} \text{ cm}^{-2})$	$3.2^{+4.0}_{-2.0}$	$4.3^{+3.5}_{-2.1}$
	C-statistic/nbins	160/838	224/1060
5	Γ	$1.59^{+0.35}_{-0.34}$	$2.33^{+0.49}_{-0.46}$
	$0.2-2 \text{ keV Flux } (10^{-14} \text{ erg s}^{-1} \text{ cm}^{-2})$	$ \begin{array}{c} 1.59_{-0.34} \\ 4.5_{-2.3}^{+2.5} \\ 6.9_{-3.2}^{+5.0} \end{array} $	$5.0_{-2.8}^{+3.5}$
	$2-10 \text{ keV Flux } (10^{-14} \text{ erg s}^{-1} \text{ cm}^{-2})$	$6.9^{+5.0}$	$1.8_{-1.1}^{-2.8}$
	C-statistic/nbins	$\frac{0.5 - 3.2}{236 / 838}$	165/1060
	,	,	,
6	Γ	$1.61^{+0.36}_{-0.35}$	$1.81^{+0.42}_{-0.37}$
	$0.2-2 \text{ keV Flux } (10^{-14} \text{ erg s}^{-1} \text{ cm}^{-2})$	$4.4^{+2.6}_{-2.6}$	$4.6^{+2.4}_{-2.3}$
	$2-10 \text{ keV Flux } (10^{-14} \text{ erg s}^{-1} \text{ cm}^{-2})$	$6.4_{-3.1}^{+4.7}$	$4.7^{+3.6}_{-2.4}$
	C-statistic/nbins	230/838	222/1060

 $[^]a$ Model 1 consists of a power-law modified by Galactic absorption. The X-ray fluxes represent unabsorbed values. $^b\mathrm{All}$ errors are for 90% confidence unless mentioned otherwise with all parameters taken to be of interest except absolute normalization.

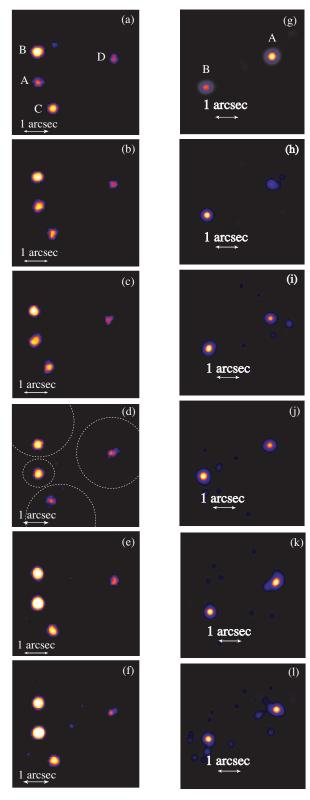


Fig. 1.— Lucy-Richardson deconvolved images in the 0.2 - 10 keV bandpass for the *Chandra* observations of RX J1131–1231 (left) and HE 1104-1805 (right). The brightness scale of the images is proportional to the count rate. The images are displayed with a linear brightness scale. East is to the left and North is up.

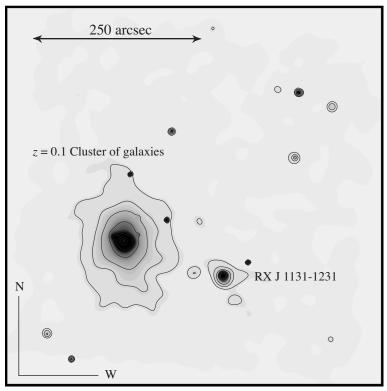


Fig. 2.— Adaptively smoothed image of the 10 ks 2004 *Chandra* observation of RX J1131–1231. To reduce background contamination and to enhance possible soft extended X-ray emission we filtered the image to include only photons with energies ranging between 0.4 and 3.0 keV.

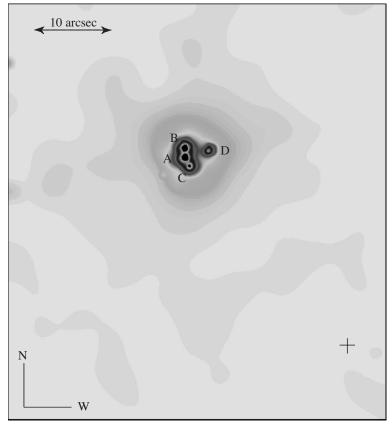


Fig. 3.— Stacked image of the six observations of RX J1131—1231 listed in Table 1. The stacked image was filtered to include only photons with energies ranging between 0.4 and 3.0 keV and adaptively smoothed. We have indicated with a cross the location of the reported, but low significance, extended X-ray emission claimed to possibly originate from a lensing cluster of galaxies. There is no indication of any extended emission.

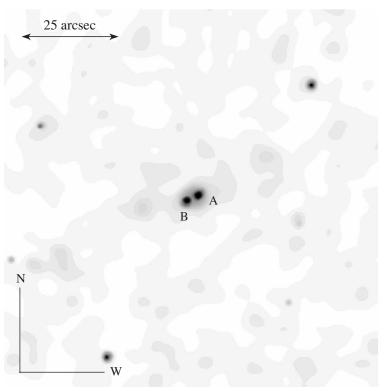


Fig. 4.— Stacked image of the six observations of HE 1104—1805 listed in Table 1. The stacked image was filtered to include only photons with energies ranging between 0.4 and 3.0 keV and adaptively smoothed. There is no indication of any extended emission originating from a group or cluster of galaxies.

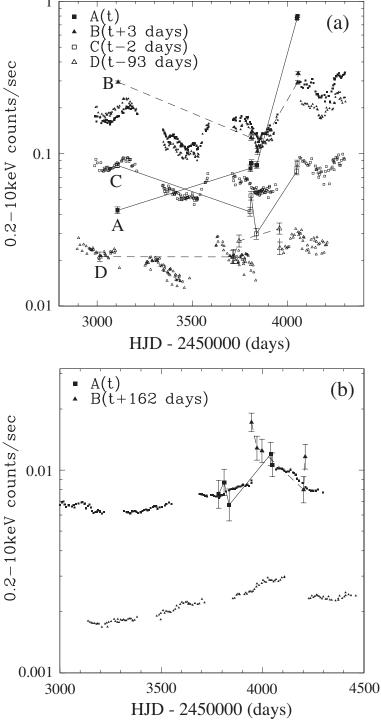


Fig. 5.— The 0.2–10 keV (large point with error bars) and R-band (small points) light curves corrected for the time delay of (a) images A, B, C and D of RX J1131–1231 and (b) images A and B of HE 1104–1805, respectively. The optical fluxes of RX J1131–1231 are normalized such that the normalized optical flux of image D is equal to the 0.2–10 keV count-rate of image D near day 3000. The optical fluxes of HE 1104–1805 are normalized such that the normalized optical flux of image A is equal to the 0.2–10 keV count-rate of image A near day $\frac{3780}{1000}$

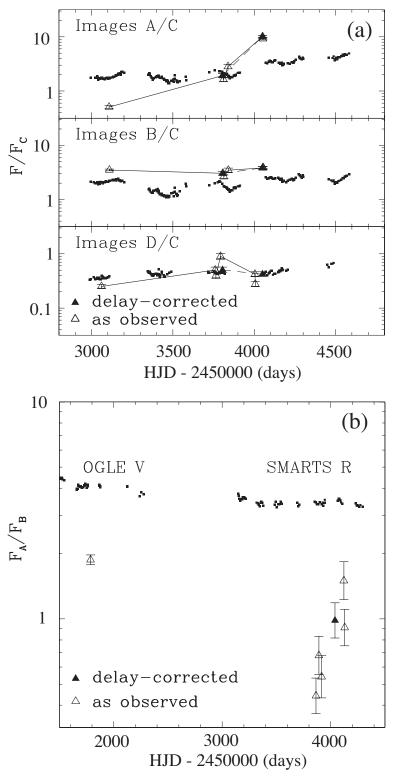


Fig. 6.— (a) X-ray (0.2–10 keV, large points) and optical (R-band, small points) flux ratios F_A/F_C , F_B/F_C and F_D/F_C for RX J1131–1231. (b) X-ray (0.2–10 keV) and optical (R-band) flux ratios F_A/F_B for HE 1104–1805. The optical flux ratios of RX J1131–1231 and HE 1104–1805 are corrected for the time-delays. The 0.2–10 keV time-delay corrected flux ratios of RX J1131–1231 and HE 1104–1805 are shown with solid triangles and the observed ratios are shown with open triangles.

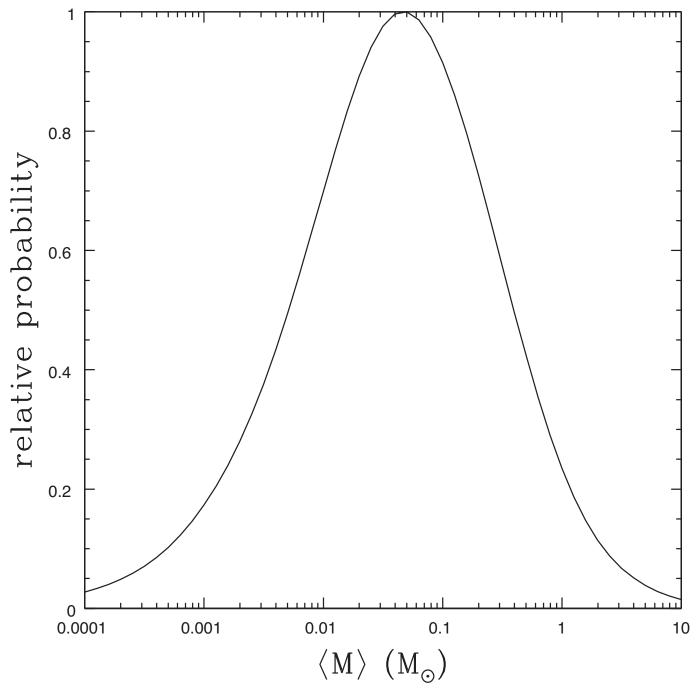


Fig. 7.— Probability density of the microlens mass scale $\langle M \rangle$ given our model for the estimated physical velocities. The peak is consistent with our alternate prior on the mass scale $(0.1 M_{\odot} < \langle M \rangle < M_{\odot})$ but broader because it is difficult to tightly constrain the mass scale using the velocities.

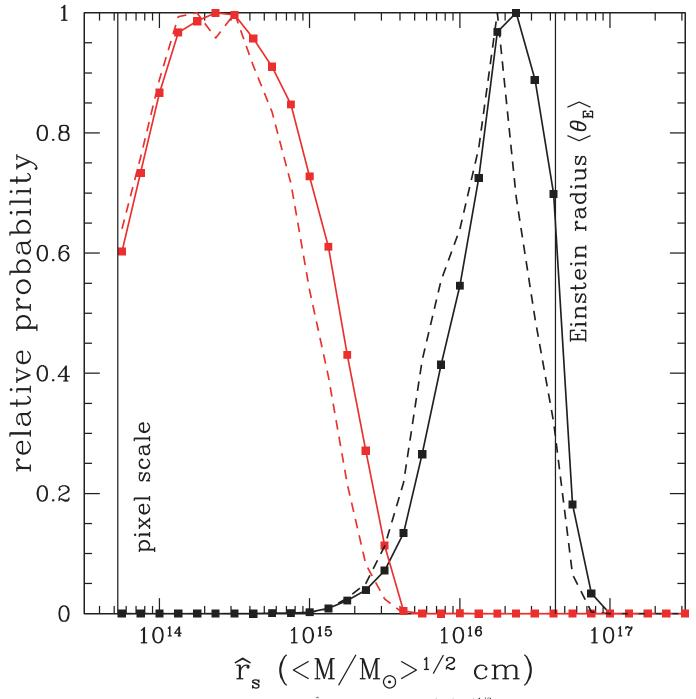


Fig. 8.— The probability density of the scaled source sizes \hat{R}_{λ} in Einstein units of $\langle M/M_{\odot}\rangle^{1/2}$ cm. Here the pixel scale and the mean Einstein radius correspond directly to the magnification patterns. The solid curves use only the velocity prior while the dashed lines add the mass prior. The mass prior eliminates low mass, high velocity, large source size solutions. Given our single X-ray data point, the probability distribution for the X-ray source would converge to a non-zero constant if we extended the calculations to still smaller sources using higher resolution magnification patterns.

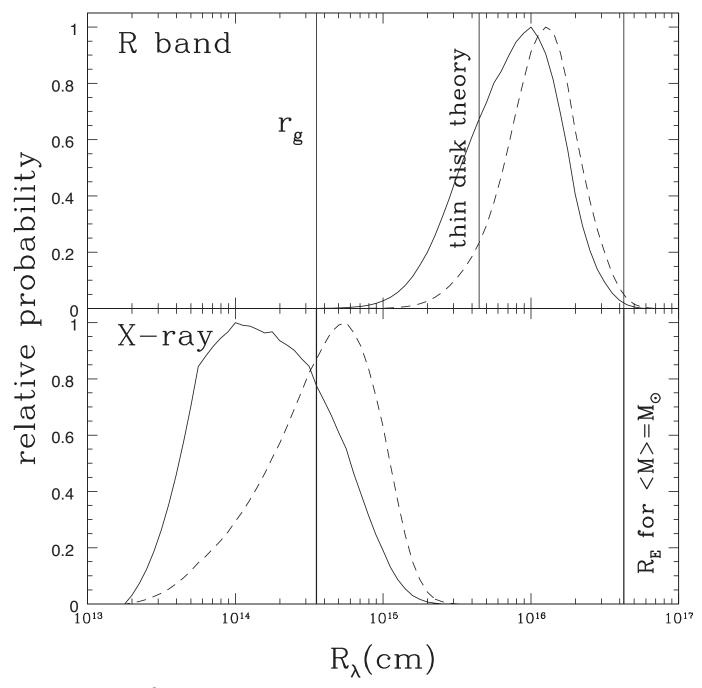


FIG. 9.— Disk size at 2000Å (top) and X-ray (bottom) for HE 1104–1805, where the solid (dashed) curves assume logarithmic (linear) priors on the source size. We show the values of R_{λ} for the assumed surface brightness profile so that the size ratios will be correct. Physically, the disk size at 2000Å can be increased by a factor of $(\cos i)^{-1/2}$ for the inclination of the disk i, and the X-ray size should be regarded as a measurement of the half-light radius with $R_{1/2}=2.44R_{\lambda}$. Vertical lines mark the gravitational radius $r_g=GM_{BH}/c^2$ and accretion disk size given the wavelength, the estimated black hole mass, and Eddington limited accretion with an efficiency of $\eta=0.1$. The final vertical line marks the Einstein radius for solar mass stars.

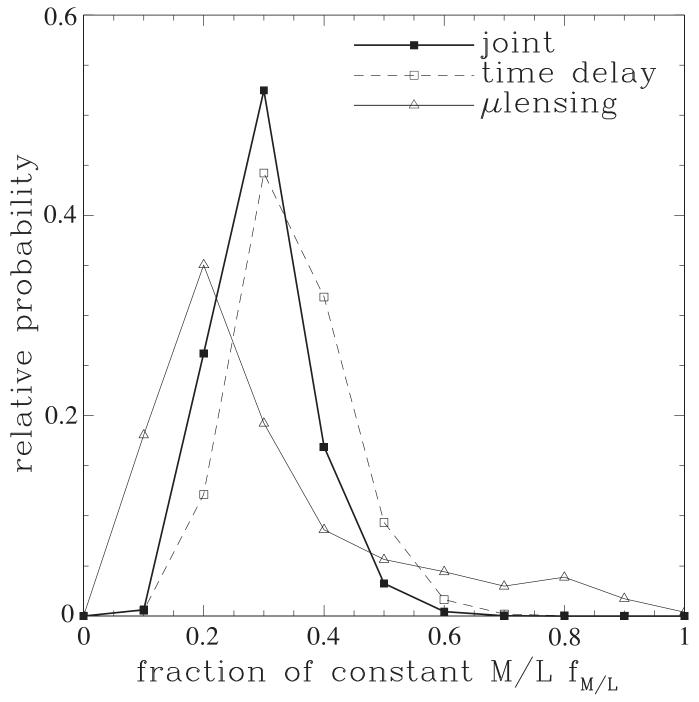


Fig. 10.— Constraints on the mass distribution. The light solid, dashed and heavy solid curves show the constraints on the mass of the stellar component of the lens mass model based on the microlensing models (heavy solid), the time delay measurements (dashed) and the combination of the two (light solid). A constant M/L model has $f_{M/L} = 1$ and a pure dark matter halo model has $f_{M/L} = 0$, with the stellar mass reduced from the constant M/L model in proportion to $f_{M/L}$

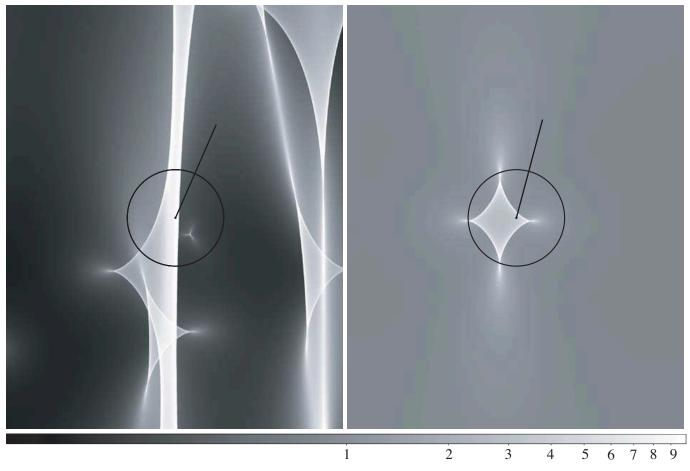


Fig. 11.— Simulated microlensing caustics for HE 1104–1805. These show small sections of one pair of the $f_{M/L}=0.3$ magnification patterns for images A (left) and B (right) where higher magnifications are white and lower magnifications are black. The lines show the path followed by the source for the period covered by the *R*-band data starting from the circled point. The large circle is the size of the UV (rest-frame) source (log $\hat{R}_{\lambda}=16.2$) and the small (almost invisible) circle is the size of the X-ray source (log $\hat{R}_{\lambda}=14.2$).

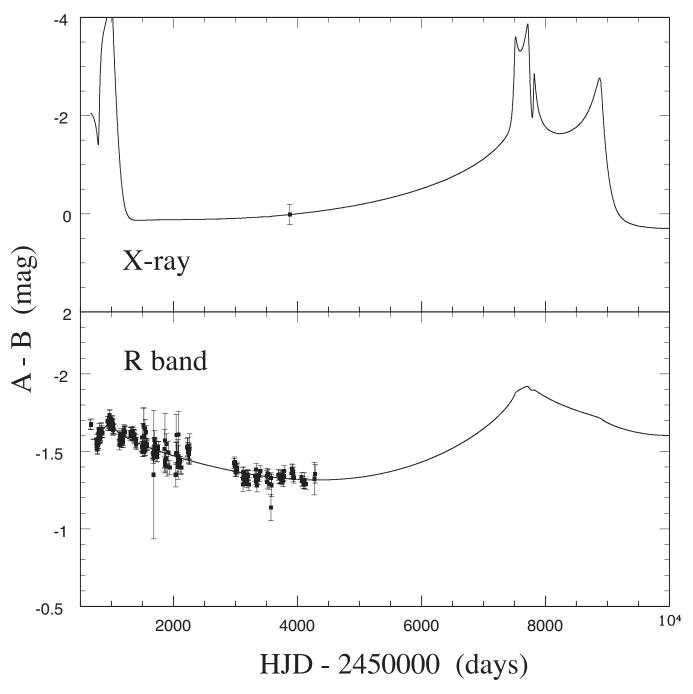


Fig. 12.— The *R*-band and X-ray magnitude differences for the trial shown in Fig. 11 as compared to the observations. This trial was chosen because it fit the data well and we found the origin of the initial peak as a pair of competing caustic crossings in the two images intriguing. The dramatic differences in the vertical scales show that an X-ray light curve of this lens should be much more dramatic than the *R*-band.